Modelling and Simulation in Materials Science and Engineering

PAPER • **OPEN ACCESS**

A numerical study of the influence of crystal plasticity modeling parameters on the plastic anisotropy of rolled aluminum sheet

OPEN ACCESS
IOP Publishing
Modelling and Simulation in Materials Science and Engineering
Modelling Simul. Mater. Sci. Eng. **28** (2020) 085005 (19pp) https://doi.org/10.1088/1361-651X/abb8e2

A numerical study of the influence of crystal plasticity modeling parameters on the plastic anisotropy of rolled aluminum sheet

M Kasemer[1,2,*], G Falkinger[3] and F Roters[2]

[1] Department of Mechanical Engineering, The University of Alabama, Tuscaloosa, Alabama, United States of America
[2] Max-Planck-Institut für Eisenforschung GmbH, Düsseldorf, Germany
[3] Austria Metall AG, Ranshofen, Austria

E-mail: matthew.kasemer@ua.edu

Received 18 May 2020, revised 19 August 2020
Accepted for publication 16 September 2020
Published 27 October 2020

Abstract

The production of stamped parts from rolled aluminum sheets requires different tempers and different thermal routes. While the slip and hardening behavior of the alloy strongly depends on the temper and the process temperature, the crystallographic texture remains largely static. Although the plastic anisotropy of rolled sheet is largely a function of the crystallographic texture, a dependency of plastic anisotropy on the temper has been reported for 6xxx series alloys, indicating that slip and hardening behavior have some influence. A systematic investigation of the effect of the slip and hardening behavior on the plastic anisotropy, however, does not exist. In this study, a crystal plasticity fast Fourier transform framework is utilized to predict the *r*-values, a common measure for plastic anisotropy, of two widely used commercial aluminum alloys possessing different crystallographic textures, AA6016 and AA5182. To investigate the sensitivity of the *r*-values to changes in the modeling parameters, a suite of simulations is performed in which the modeling parameters are systematically changed, and the resulting changes to the predicted *r*-values are calculated. Furthermore, numerical parameters, such as the level of discretization and the number of simulated grains are studied. Results indicate that

*Author to whom any correspondence should be addressed.

the predicted *r*-value is less dependent on changes to crystal plasticity modeling parameters than to the initial crystallographic texture. Resulting trends are discussed.

Keywords: rolled aluminum, plastic anisotropy, crystal plasticity, deformation modeling

(Some figures may appear in colour only in the online journal)

1. Introduction

Aluminum alloys are often used in various engineering applications, as they are lightweight, resist corrosion, and exhibit desirable mechanical properties for use in forming operations. Increasingly, aluminum is sought after for use in automotive and aerospace industries in an attempt to exploit these properties. Worldwide demand for aluminum auto body sheets is projected to increase from 0.5 million tons in 2013 and 1.6 million tons in 2018 to 3.8 million tons in 2027. The increase is mainly driven by the substitution of other materials with aluminum sheets [1].

Automotive body parts require high strength and excellent formability. The latter is severely affected by the plastic anisotropy of rolled sheet [2–4]. Typical technical specifications for aluminum sheets by automobile manufacturers [5] therefore limit the extent of plastic anisotropy exhibited by rolled aluminum sheets. The most common metric to quantify the plastic anisotropy is the so called '*r*-value' (sometimes referred to as the Lankford coefficient), which relates the magnitude of the plastic strain in the sample's thickness direction and the magnitude of the plastic strain across the width of a sample [6, 7]. Depending on the crystallographic texture of the rolled sheet, the *r*-value may be variable as a function of the sample's orientation with respect to the sheet's loading direction [7–9]. The plastic behavior—and thus the *r*-value—of rolled sheets tends to be highly dependent on their crystallographic texture. For Al–Mg–Si alloys a small but significant effect of age hardening [10] and natural hardening [11] on the *r*-value has been found. These effects are not yet fully understood but might be related to the interplay of hardening mechanisms on different slip planes [12, 13]. In other words, there are some indications that the tempering of rolled sheet—and resulting changes of the hardening behavior—has some influence over the plastic anisotropy.

The relatively recent development of the full-field crystal plasticity simulation method has allowed for the better prediction of both micro- and macroscopic behavior of materials [14]. These simulations explicitly consider both the crystallographic texture and the three-dimensional geometric character of a microstructure for a given sample. Simulations are commonly evaluated via either a crystal plasticity finite element solution method [15–17], or a crystal plasticity fast Fourier transform (FFT) solution method [18–20]. By modeling the single crystal deformation response as well as considering the spatial arrangement of grains and phases (neighboring grain interaction), a better understanding of the macroscopic plastic deformation response—and the influence of the plastic response at the crystal scale—can be achieved. Comparative studies of computational approaches with increasing complexity by Delannay *et al* [21] and Hu *et al* [22] showed that full-field methods based on three-dimensional representations of the micro-structure yield the best predictions for the bulk behavior such as texture evolution and plastic anisotropy.

Full-field crystal plasticity simulations require—generally at a minimum—input pertaining to a sample's microstructure (geometry and crystallographic texture), and the single crystal elastic and plastic behavior. Texture measurements of specimens via electron backscatter

Table 1. Chemical composition in wt% for aluminum alloys AA6016 and AA5182 utilized in this study.

Alloy	Fe	Mg	Mn	Si	Al
AA6016	0.13	0.35	0.07	1.02	Balance
AA5182	0.19	4.73	0.43	0.12	Balance

diffraction or lab-source x-ray diffraction have become commonplace, and analysis has become readily accessible via open-source tools [23]. Single crystal elastic and plastic parameters for use in crystal plasticity simulations, however, can be difficult, time-consuming, and costly to accurately quantify [24, 25]. As full-field modeling becomes more accessible and widely adopted—especially in industrial applications—an understanding of the influence of modeling parameters on the deformation response is necessary to inform the modeler on the necessity (or lack thereof) of accurate parameter quantification. Various studies have shown that great care needs to be taken with respect to parameter estimation when investigating the intra-grain deformation response of polycrystalline materials [26, 27]. To date, however, there has been little work on understanding the sensitivity of the prediction of bulk behavior on changes to crystal plasticity modeling parameters.

In this study, a full-field crystal plasticity solver is used to predict the *r*-value of two aluminum alloys—AA6016 and AA5182. Multiple samples for each alloy are generated, and different loading cases are considered. Various modeling parameters—namely slip and hardening parameters, the level of numerical discretization, the number of grains in a sample (the geometric discretization), and the initial crystallographic texture (both the texture differences between the two alloys, and through-thickness texture gradients)—are parameterized, and a suite of simulations is performed in which each parameter is systematically altered to study it is influence on the predicted *r*-value. Resulting trends as a function of changes to the modeling parameters are examined, and the impact of such trends discussed.

2. Materials and methods

2.1. AA6016 and AA5182 sheet alloys

The commercial aluminum alloys AA6016 and AA5182 in this study are typical for stamped parts in automobiles. Their chemical composition is given in table 1.

The texture of AA6016 is generally dominated by the cube texture component [28]. During hot rolling, cube oriented grains grow at the expense of other orientations [29]. Cold rolling and subsequent solution annealing further strengthens the cube texture component [30, 31]. The propensity of the cube texture component to form originates from a complex micro-mechanism. While cold rolling promotes the brass, copper and S texture components and reduces the cube texture component, far more stable recrystallization nuclei are created during rolling with cube orientations than with any other orientation [32, 33]. As a consequence, AA6016 sheets typically exhibit a strong cube component in the final fully recrystallized state.

Compared with AA6016, the AA5182 alloy is comprised of a significant number density of micron-sized AlMnFe particles, and a high content of solute Mg-atoms. The deformation zones around the second-phase particles (which arise during rolling) are preferential nucleation sites, thus creating randomly oriented recrystallization nuclei [34]. This so-called ‘particle stimulated nucleation’ (PSN) competes with the cube orientation nucleation during recrystallization [35]. The high solute content additionally reduces the cube advantage [36]. Both PSN and the

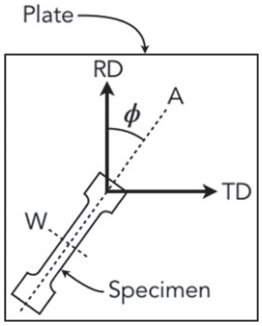

Figure 1. Illustration of a rolled sheet and tensile specimen. The sheet is defined via the processing directions: the rolling direction, RD, and transverse direction, TD, and a third out of plane normal direction, ND. The specimen orientation is defined via the orientation of the specimen's tensile axis, A, with respect to the sheet's rolling direction, quantified as the angle ϕ.

presence of solute magnesium retard the development of a strong cube texture component and lead to a mixture of retained rolling texture components and the cube texture component in the final fully recrystallized sheet.

Samples in this work have been extracted from commercial sheets produced at AMAG Rolling GmbH. The microstructure of both alloys is fully recrystallized. The alloy AA6016 has been solution annealed in a continuous heat treatment line and subsequently water quenched (a T4 temper). The alloy AA5182 has been annealed in a batch furnace and subsequently air cooled (an O temper).

2.2. Determination of r-value

The r-value is typically determined via a tensile test at a certain angle to the rolling direction (figure 1). The strains are measured in both the loading direction and across the width of the sample (perpendicular to the loading direction). The strain across the thickness of the sample is derived from the condition of volume conservation. This study largely adheres to the calculation of the r-value as described in ISO standard 10 113 [6]. In this standard, the true plastic logarithmic strains in the loading direction, ϵ_A, and across the width of the sample, ϵ_W (corresponding to axes 'A' and 'W', respectively, in figure 1) are collected continuously during loading. Data points within a window from 8% to 12% strain in the loading direction are fitted by linear regression. The slope of the regression line, m, is related to the r-value, r, via:

$$r = -\frac{m}{1-m}. \tag{1}$$

This is illustrated in figure 2. In contrast to the ISO standard (pictured), in this study, the regression line is not required to pass the origin—that is, a linear regression is applied to only the data between 8% and 12% strain. This modified procedure is used to calculate the r-value from both the experimental data and the simulated data.

To quantify the plastic anisotropy of the alloys in this study, tensile tests were carried out on a Zwick Z100 tensile machine according to the ISO 6892-1 standard [37] at a strain rate of 0.0067 per second. Tensile specimens with an initial width of 20 mm and a gauge length of 80 mm were extracted from the center of the sheets at angles (ϕ, figure 1) of 0°, 22.5°, 45°, 67.5°, and 90° to the rolling direction. Five specimens were extracted from each sheet at each

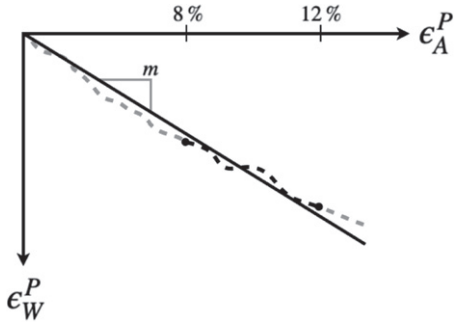

Figure 2. Calculation of slope, m, used in r-value calculation of ISO 10113. Experimental plastic strains are measured (dashed lines), and a linear regression (dark solid line) is performed in which the data points between axial plastic strains of 8% and 12% are considered (dark dashed line). In the standard, the linear regression is forced to intersect the origin, though this constraint is not enforced in the present study. This figure is adheres to the standard in [6].

inclination. The sheet thickness of the AA6016 and AA5182 alloys is 1.25 mm and 1.7 mm, respectively.

2.3. Texture measurement

EBSD scans were performed on a Zeiss XB1540 with a Hikari detector, utilizing an electron beam energy of 15 kV and a 5 × 5 binning mode. Scans are performed over the entire through-thickness of the sheet samples to allow for the measurement of the grain structure and texture of both the bulk material and selected regions through the thickness of the sheet. EBSD measurements are plotted in figure 3. Qualitatively, grains in both scans are largely equiaxed and homogeneous—that is, no indication of preferential elongation in any directions, with little discernible intra-grain orientation gradient (at least at this resolution).

The EBSD data is used to calculate the crystallographic texture of the sheets. The bulk texture of the entire through-thickness is represented via pole figure stereographic projections, shown in figure 4. As detailed, the experimentally deduced textures are as expected for the two alloys—that is, a texture dominated by the cube component for the AA6016 sample, and a texture with retained rolling components for the AA5182 sample (see: section 2.1). Note the strengths of the textures for the two samples are not particularly strong—with a maximum peak component of 2.7 multiples of unity distribution (MUD) at the cube component for the AA6016 sample, and 1.7 MUD at the brass component for the AA5182 sample. Pole figures are plotted via the MTEX toolbox [23].

2.4. Crystal plasticity modeling

The model employed in this study considers the elastoplastic deformation response of single crystals. The elastic portion of deformation considers elastic anisotropy, and plasticity is modeled via a restricted slip rate dependent phenomenological power law with a saturation style hardening model. Within a domain, a regular grid of material points is constructed. Each material point is considered to represent a single crystal, and an ensemble of material points in three dimensions a polycrystal (where, generally, a grain consists of multiple material points). The model employed in this study is ductile and isothermal, and does not consider other modes

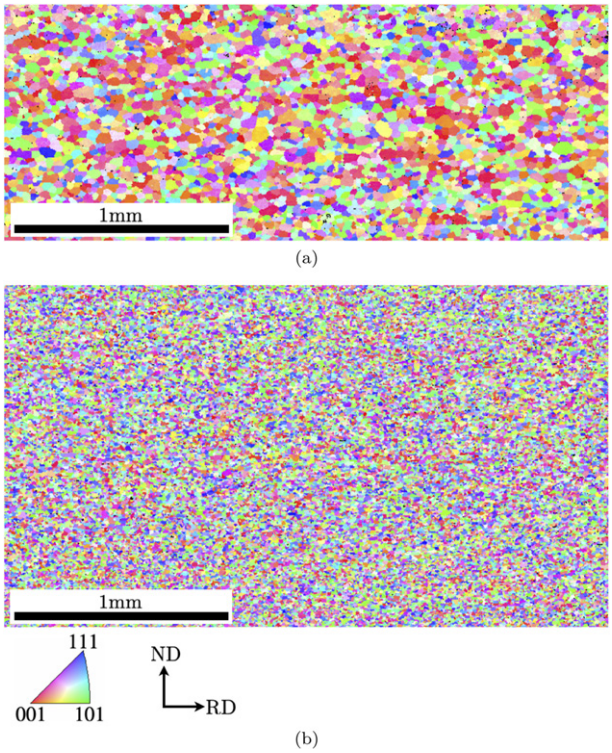

Figure 3. EBSD scans through the thickness of the sheet (in the RD/ND plane) for the (a) AA6016 sample, and (b) AA5182 sample. IPF color map is in reference to the sample's rolling direction (RD). Note the differences between the height of the images, corresponding to the final thicknesses of the rolled sheets (nominally 1.24 mm and 1.74 mm, respectively).

of plastic deformation (i.e., twinning). For sake of brevity, an abridged description appears below. A full description of the kinematics, constitutive models, and implementation can be found in [20].

Anisotropic single crystal elasticity is modeled via Hooke's law, which relates the Green–Lagrange strain, $\mathbf{E}$, to the second Piola–Kirchhoff stress, $\mathbf{S}$, via the anisotropic elastic stiffness tensor, $\mathbb{C}$:

$$\mathbf{S} = \mathbb{C}\mathbf{E}. \tag{2}$$

The stiffness tensor is reduced to reflect the symmetry of the crystal [38], in this case cubic.

Plasticity is governed by a rate dependent restricted slip model,

$$\dot{\gamma}^{\alpha} = \dot{\gamma}_0^{\alpha} \left| \frac{\tau^{\alpha}}{\xi^{\alpha}} \right|^{n} \operatorname{sgn}\left(\tau^{\alpha}\right). \tag{3}$$

Here, $\dot{\gamma}_0$ is the fixed-state strain rate scaling coefficient, τ is the resolved shear stress, ξ is the slip system strength (or resistance to shear), all on the αth slip system. Note that ξ is initialized equally for all slip systems of a given slip family (ξ_0). In this study, only the dominant $\{111\}\langle 01\bar{1}\rangle$ family of slip systems is considered.

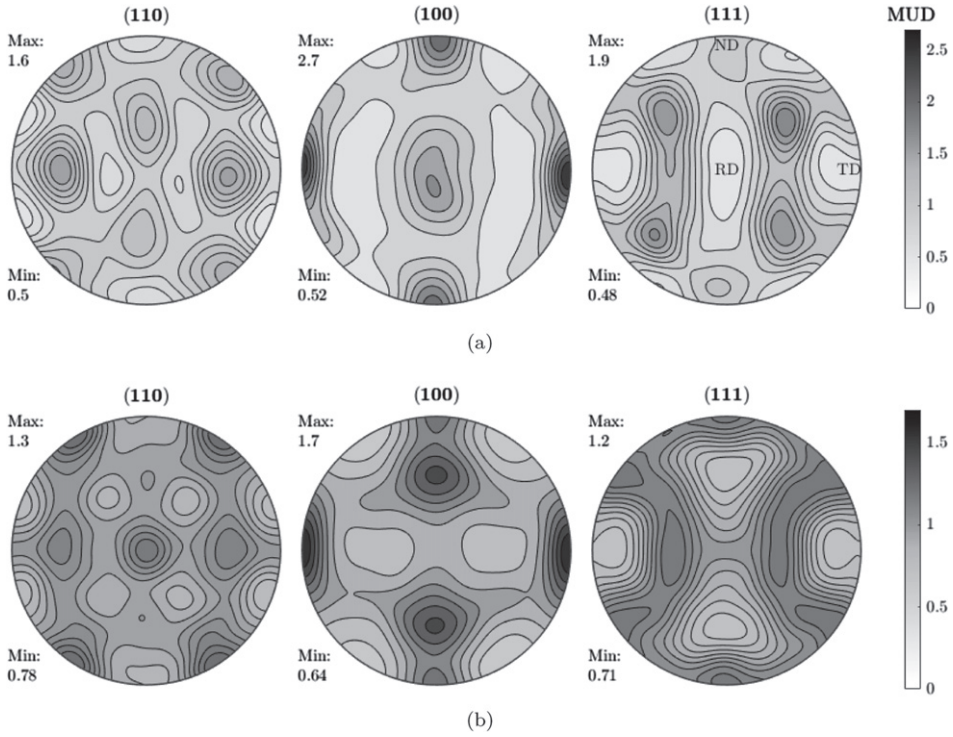

Figure 4. Crystallographic texture (in units of MUD, or multiples of unity distribution) calculated from EBSD measurements plotted on pole figure stereographic projections for the (a) AA6016 sample (processing directions specified in the (111) pole figure), and (b) AA5182 sample. Note how the AA6016 sample exhibits an overall stronger texture than the AA5182 sample, as evidenced by the differences in color scaling. Plotted via the MTEX toolbox [23].

The strength of each slip system evolves via a saturation model,

$$\dot{\xi}^{\alpha} = h_0 \sum_{\beta=1}^{N_S} \left|\dot{\gamma}^{\beta}\right| \left|1 - \frac{\xi^{\beta}}{\xi_{\infty}^{\beta}}\right| \operatorname{sgn}\left(1 - \frac{\xi^{\beta}}{\xi_{\infty}^{\beta}}\right) h_{\alpha\beta}, \tag{4}$$

where h_0 is the strength hardening rate coefficient, N_S is the number of slip systems (12 for the $\{111\}\langle 01\bar{1}\rangle$ family of slip systems), and ξ_{∞} is the slip system saturation strength. The interaction between a given slip system, α, and other slip systems, β, is considered via the interaction matrix, $h_{\alpha\beta}$, which allows for the selection of various hardening assumptions (i.e., isotropic, direct, and latent hardening).

An FFT method is employed to numerically approximate the solution, implemented in the DAMASK software package [20]. Implementation is not described in this paper. Boundary conditions are applied as volume averages–that is, a target average deformation gradient is set for the entire volume. Local deformation gradients are solved iteratively to satisfy the global average. It is worth noting that inherent in the FFT solution method is the necessity of periodic boundary conditions. In other words, the applied macroscopic deformation is assumed periodic in the directions of the sample basis. Consequently, the geometric morphology of the polycrystal is forced to be periodic in the sample directions. Boundary conditions are explained in full in [20].

Table 2. Anisotropic single crystal elastic constants for fcc aluminum.

$\mathbb{C}_{11}$ (GPa)	$\mathbb{C}_{12}$ (GPa)	$\mathbb{C}_{44}$ (GPa)
106.75	60.41	28.34

Table 3. Plasticity parameters for fcc aluminum.

$\dot{\gamma}_0$ (m s^{-1})	n	h_0 (MPa)	ξ_0 (MPa)	ξ_∞ (MPa)	$h_{\alpha\beta}$ ($\alpha \neq \beta$)
0.001	20	75	31	63	1.4

When modeling *r*-values, the loading is generally fixed and the grain orientations are transformed to mimic changes in texture with respect to the loading direction. In this study, the loading is changed with respect to a fixed microstructure. Since boundary conditions are applied as macroscopic average deformation gradients, different loading conditions are readily applied. The applied macroscopic boundary condition, $\mathbf{F}_{\text{BC}}$, is altered via a rotation matrix, $\mathbf{R}_{\text{BC}}$, via the transformation:

$$\mathbf{F}_{\text{app}} = \mathbf{R}_{\text{BC}}\mathbf{F}_{\text{BC}}\mathbf{R}_{\text{BC}}^{\text{T}}, \tag{5}$$

where $\mathbf{F}_{\text{app}}$ is the resulting applied deformation gradient, and $\mathbf{R}_{\text{BC}}$ represents the rotation representing some in-plane inclination of the sample. In this way, different macroscopic loading conditions can be applied to a single microstructure. This allows for grain neighborhoods to remain constant as different loading conditions are applied.

Base elasticity and plasticity parameters are chosen for the dominant crystallographic phase, as they represent the behavior of generic aluminum alloys [39, 40]. Elasticity parameters are summarized in table 2, and plasticity parameters in table 3.

2.5. Simulation suite

To judge the sensitivity of the predicted *r*-value to changes in simulation parameters, a suite of simulations is performed in which certain simulation parameters are systematically altered. In this study, changes to the initial slip system strength, ξ_0, the slip system saturation strength, ξ_∞, the hardening assumption (via the slip interaction matrix, $h_{\alpha\beta}$), the rate dependence, n, the degree of numerical discretization (the number of material points in a domain), the number of grains in a domain (or the geometric discretization), and the initial crystallographic texture are considered. Elastic parameters are fixed in this study. A base parameter set is chosen, comprised of the modeling parameters shown in tables 2 and 3, a numerical discretization of 32^3 voxels, a geometric discretization of 1000 grains, and an initial texture representing the bulk sample (i.e., the entire through-thickness). For the plasticity parameters, numerical discretization, and geometric discretization, values are systematically altered to values higher (double) and lower (half) than the base values. Changes to these values are summarized in table 4. Note that changes of this magnitude to the plasticity parameters are extremely large—beyond what is normally utilized to model the deformation response of aluminum alloys. Changes to the numerical discretization and geometric discretization are within bounds that reflect typical modeling criteria.

The hardening assumption is parameterized via the adjustment of hardening interaction parameters in the matrix $h_{\alpha\beta}$. The base hardening assumption is that in which each slip system self hardens, while activity on its in-plane neighbors contribute to its own hardening at a relatively more rapid rate (1.4x) [20]. In addition, both full self hardening and full latent hardening assumptions are employed. In the full self hardening assumption, the hardening interaction

Table 4. Base simulation parameters and changes in parameters. Note that a total of eleven parameter sets are described in this table: 1 using the base parameters, and 5 each for lower and upper bound changes to each of the modeling parameters. Changes to the hardening assumption (full self hardening and full latent hardening) and to texture sampling (top of sample, middle of sample, and intermediary) are also considered, accounting for an additional 5 parameter sets.

Parameter	Base value	Lower bound	Upper bound
ξ_0 (MPa)	31	15.5	62
ξ_∞ (MPa)	63	31.5	126
n	20	10	40
Material points	32^3	10^3	64^3
Grains	1000	500	2000

matrix becomes identity—that is, each slip system hardens only due to its own slip activity. In the full latent hardening assumption, the hardening interaction matrix is populated entirely with unity values except for the diagonal, which is populated by zeros—that is, each slip system hardens only due to activity on other slip systems.

Orientation sets are randomly sampled from the list of crystallographic orientations indexed via EBSD. Direct sampling is utilized over other methods—such as calculating and sampling an orientation distribution function—to avoid possible bias or under-representation of the true texture. Direct sampling is appropriate to represent the overall texture of the sheet due to the large amount of grains indexed in both EBSD scans. For the base sets of orientations, grain orientations are randomly selected from the entire list of indexed orientations, and thus the texture matches the bulk texture of the entire sheet volume. Consequently, we do not retain any through-thickness texture gradients in the base orientation sets. To provide statistics of the predicted sheet behavior, ten different orientation sets are generated for each alloy. To determine the effect that through-thickness texture gradients may have on the predicted r-value, orientation sets are generated using grains indexed in specific regions of the through-thickness profile. Figure 5 details the three regions considered—one considering grains near the surfaces of the sheets, one considering grains near the center of the sheets, and one considering grains in an intermediary region. Again, ten different orientation sets are generated for each alloy and each region considered to provide statistics for the predictions.

With the exception of changes in the initial slip system strength, only one parameter is changed at a time. For simulations in which the initial slip system strength is variable, the slip system saturation strength is also changed to retain the same available magnitude of hardening ($\xi_\infty - \xi_0$) as the base parameter set (32 MPa). Specifically, when the initial slip strength is doubled (to 62 MPa), the saturation strength is increased (to 94 MPa) to keep the magnitude of hardening consistent. Similarly, when the initial slip strength is halved (to 15.5 MPa), the saturation strength is decreased (to 47.5 MPa). For simulations in which the saturation strength is variable, the initial strength is held constant at the base value.

Grain morphology is represented via a periodic Voronoi tessellation. Sensitivity to the geometric morphology of the microstructure is not considered in this study, and thus only a single geometric morphology is used. Figure 6 (plotted via ParaView [41]) details a domain discretized into 1000 grains utilizing numerical discretization levels of 10^3, 32^3, and 64^3 material points. Note the refinement of the grain morphology as the level of numerical discretization is increased. As stated in section 2.4, the geometric morphology of the microstructure is forced to be periodic in the directions of the sample basis, to be consistent with the applied boundary

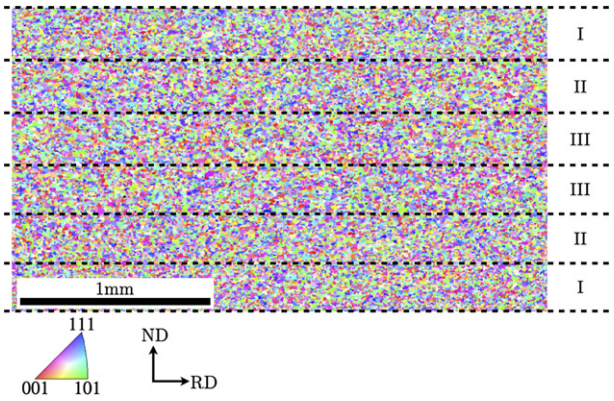

Figure 5. EBSD scan for the AA5182 sample detailing the approximate boundaries used to selectively sample orientations to test the effects of through-thickness texture gradient. Region I considers grains near the surfaces of the sample, while region III considers grains near the center of the sample. Region II considers grains in the intermediary region. Proportional boundaries are used for the AA6016 sample (figure omitted due to sake of brevity).

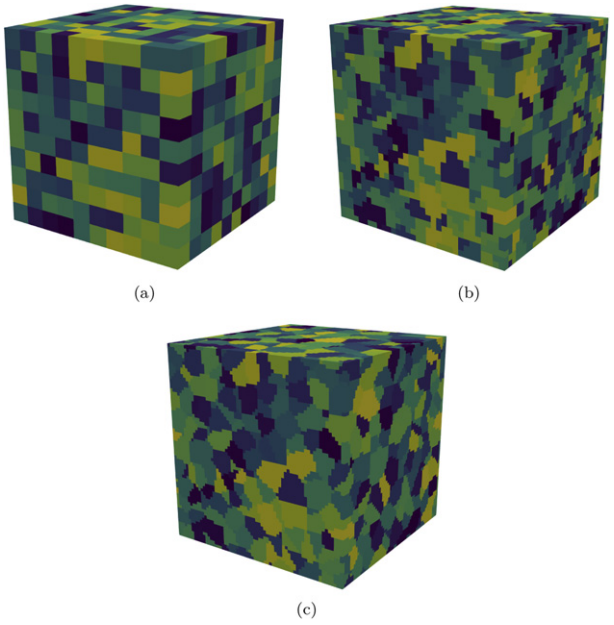

Figure 6. Example grain morphologies for samples containing 1000 distinct grains, numerically discretized using (a) 10^3, (b) 32^3, and (c) 64^3 material points. Grains are colored arbitrarily. Plotted via ParaView [41].

conditions. In this study, minor crystallographic phases are ignored owing to their relatively small volume fraction.

A total of 1600 simulations are performed (due to the computational efficiency, no design of experiments was used, and instead all simulations across all variables considered were performed). One base parameter set, upper and lower bound sets for 5 parameters (for ξ_0, xi_∞, n, number of material points, and number of grains), 2 additional hardening assumptions, and three additional crystallographic textures are considered, for a total of 16 parameter sets. Each parameter set is simulated 100 times—considering two different crystallographic textures (samples), ten orientation sets from each texture, and five different loading cases to match those from the experimental tests (corresponding to five different in-plane inclinations of 0°, 22.5°, 45°, 67.5°, and 90°, considered via the rotated boundary condition, $\mathbf{F}_{\text{app}}$, described in the preceding section).

Note: completion of all 1600 simulations and post-processing analysis took approximately 168 h on a computational workstation with 2 Xeon Gold 6150 processors containing 18 cores each (36 cores total). Simulations were performed in parallel utilizing the entirety of the workstation's processor resources.

3. Results and discussion

Results of the simulation suite are shown in figures 7–14. Plots depict changes in the r-value as a function of changes in modeling parameters. Specifically, for a given set of modeling parameters and a given loading direction (in-plane inclination), the mean value over the ten orientation sets is plotted, with error bars denoting the standard deviation in the predicted r-value for those ten simulations. For instance, in figure 7, the solid circle at $\phi = 0$ shows that for the ten simulations (for the different orientation sets, or samples) performed with no in-plane inclination, the mean r-value was calculated to be approximately 0.83, with a standard deviation of approximately 0.5.

To quantify the degree of sensitivity of the r-value to changes in modeling parameters, the maximum and minimum absolute differences between high and low parameter sets are determined for each sample. For a given variable parameter, the differences are calculated as:

$$\begin{aligned} \Delta r^{\max} &= \max \left| r^i_{\text{high}} - r^i_{\text{low}} \right| \\ \Delta r^{\min} &= \min \left| r^i_{\text{high}} - r^i_{\text{low}} \right|, \end{aligned} \tag{6}$$

performed at the ith in-plane inclination, and high and low refer to the r-values calculated using the high and low values for a given parameter set. These values are summarized in table 5, which lists the loading direction (in-plane inclination) at which the maxima and minima occur.

Compared to experimental values (figure 7), the simulations are able to capture the general trends of the r-value with respect to changes in the loading direction, and changes in crystallographic texture. It should be noted that there is not an exact match between simulation and experiment. However, as the purpose of this study was to identify the role of modeling parameters in predicting the r-value rather than attempting to directly recreate the experiments, various assumptions were made (i.e., generic anisotropic elastic constants, no consideration of a second minor crystallographic phase).

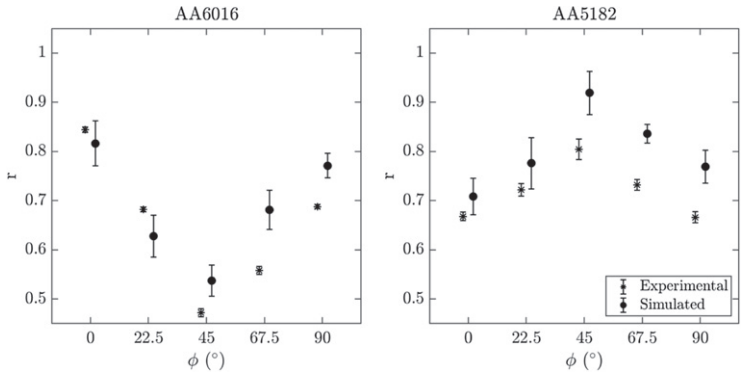

Figure 7. Comparison between experimental and simulated *r*-values using base simulation parameters. Error bars depict the standard deviation of the *r*-value for the sets of experiments or simulations performed at each in-plane inclination, ϕ. Note: experiments were conducted with 5 specimens at each in-plane inclination, while simulations were conducted with 10 specimens at each in-plane inclination.

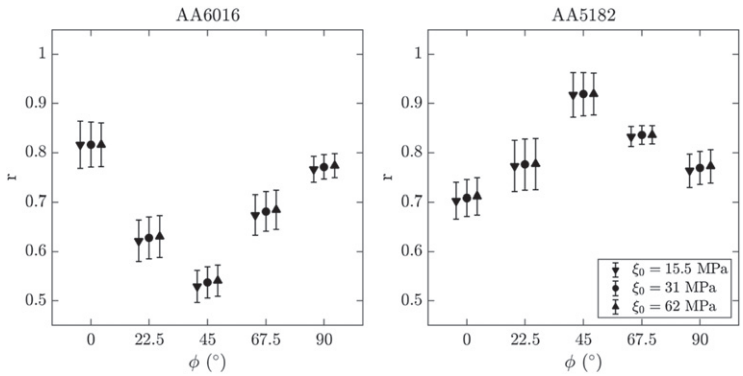

Figure 8. Simulated *r*-values for changes in the initial slip system strength, ξ_0. Error bars depict the standard deviation of the *r*-value for the sets of simulations performed at each in-plane inclination, ϕ.

3.1. Effect of hardening parameters

Overall, the average predicted *r*-value tends to increase for the simulations in which the initial slip system strength (ξ_0) is increased and decreases in the simulations in which the slip system saturation strength (ξ_∞) is increased (figure 9). Both effects, however are small and the maximum change of the *r*-value is 0.01 for the saturation stress and the initial yield stress. A larger effect was found for the rate-sensitivity exponent. The average predicted *r*-value tends to increase when the rate exponent *n* is increased. The maximum change of the *r*-value is 0.025. The largest sensitivity was found for the latent hardening. The average predicted *r*-value tends to increase when the latent hardening ($h_{\alpha\beta}$ where $\alpha \neq \beta$) is decreased and a maximum difference of *r*-values of 0.03 was determined. For latent hardening, a similar trend was observed by other authors [42] as well.

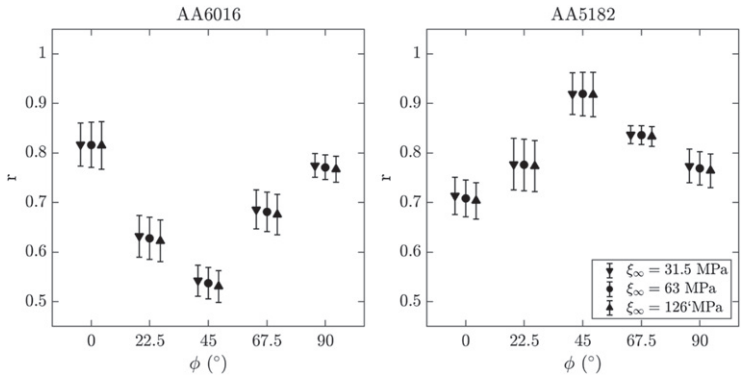

Figure 9. Simulated *r*-values for changes in the slip system saturation strength, ξ_∞. Error bars depict the standard deviation of the *r*-value for the sets of simulations performed at each in-plane inclination, ϕ.

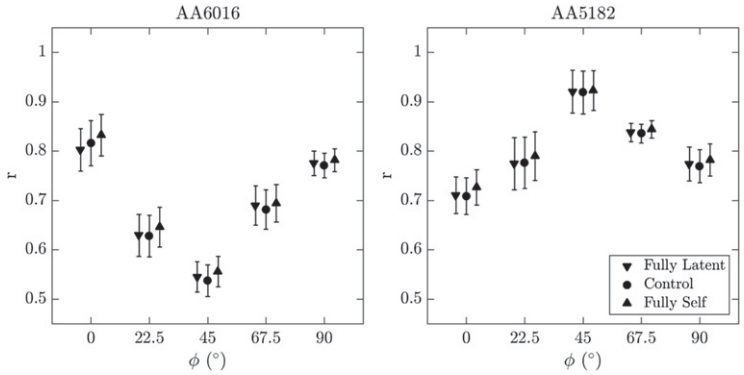

Figure 10. Simulated *r*-values for changes in the hardening assumption. Error bars depict the standard deviation of the *r*-value for the sets of simulations performed at each in-plane inclination, ϕ.

The comparison of AA6016 and AA5182 shows, that the *r*-value sensitivity itself depends on the crystallographic texture. AA6016, which has a more pronounced texture with a strong cube component, is generally more sensitive to changes in the hardening parameters than the rather balanced texture of AA5182. The absolute values of this sensitivity study might be therefore higher for highly textured materials such as 6xxx series extrusions.

The fact that the change of hardening assumption produces the most discernible results with regard to plasticity parameters is not unexpected. Since the *r*-value is related to what slip systems are active (and to what degree they are active), any changes to how those slip systems may activate can have an impact on the overall deformation response of the material [43]. The interaction of slip systems (non-zero off-diagonal terms of $h_{\alpha\beta}$) means that active slip systems may contribute to the hardening of non-active slip systems, potentially restricting or delaying their activity. Additionally, if two slip systems are active, both of their hardening rates are increased beyond their own hardening rate, leading to more rapid strength saturation. These phenomena will result in increased anisotropy of the single crystal yield surface (SCYS), and thus the

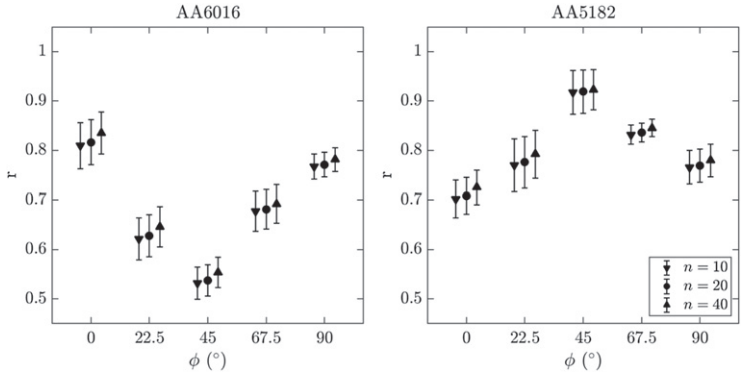

Figure 11. Simulated r-values for changes in the rate dependence of the slip kinetics, n. Error bars depict the standard deviation of the r-value for the sets of simulations performed at each in-plane inclination, ϕ.

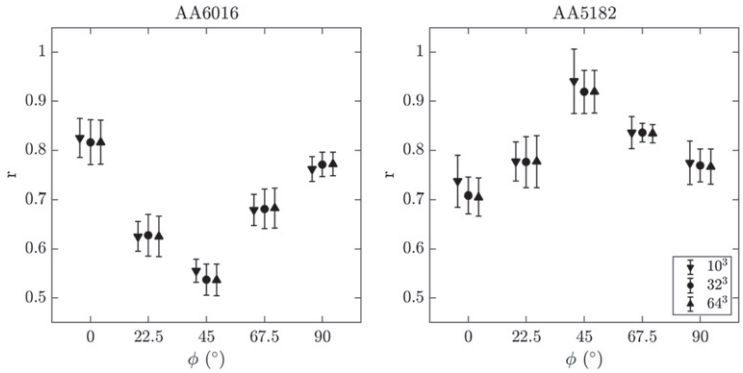

Figure 12. Simulated r-values for changes in the number of material points used to numerically discretize the domain of the polycrystalline aggregate. Error bars depict the standard deviation of the r-value for the sets of simulations performed at each in-plane inclination, ϕ.

resulting yield surface of the polycrystal—though only early in deformation (when plasticity is most transient, in the late elastic regime and early plastic regime). At some macroscopic strain state, slip systems will saturate and the SCYS of individual grains will be similar regardless of hardening assumption (the amount of available hardening does not change for each hardening assumption). In this study, the r-value is calculated well into the plastic regime, at which point these transient effects have likely reached steady state—explaining the small (though significant) effect of the hardening assumption (one could hypothesize that if the r-value were calculated closer to the point of macroscopic yield, the hardening assumptions may have a more pronounced effect).

3.2. Effect of numerical discretization

Considering the behavior due to changes in numerical discretization, results are as expected. As the number of material points is increased within a domain, and thus as the intra-grain

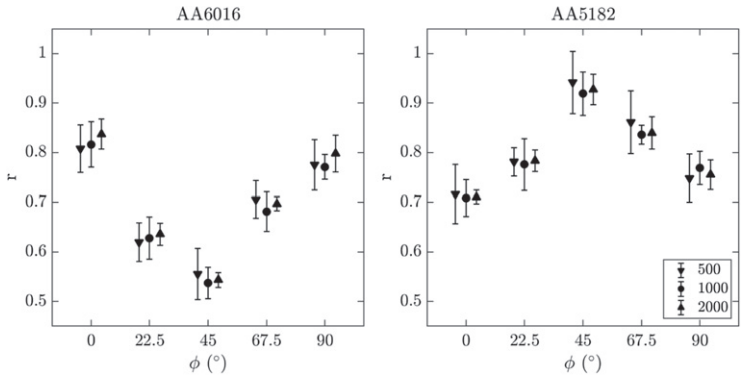

Figure 13. Simulated r-values for changes in the number of grains within the domain of the polycrystalline aggregate. Error bars depict the standard deviation of the r-value for the sets of simulations performed at each in-plane inclination, ϕ.

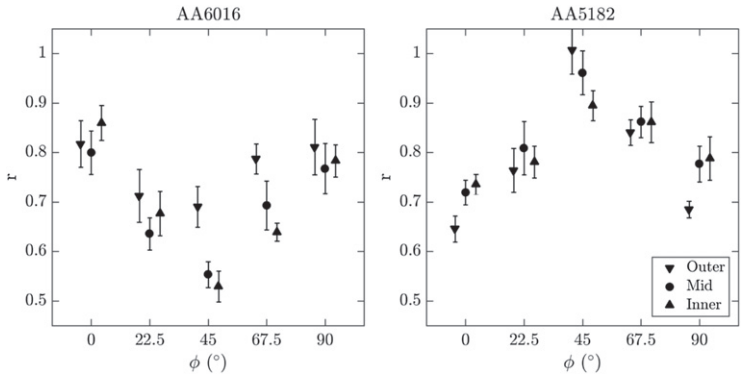

Figure 14. Simulated r-values for changes in the crystallographic texture as a function of the sampling area from the through-thickness EBSD scans, where outer, mid, and inner refer to regions I, II, and III depicted in figure 5. Error bars depict the standard deviation of the r-value for the sets of simulations performed at each in-plane inclination, ϕ.

refinement is increased, we expect the predicted response to reach a steady state, or saturate. Note how in figure 12 there is a change between the simulations performed with a low number of material points (10^3) and the base set (32^3), but little change between the base set and the high number of material points (64^3). This indicates that the average predicted bulk response has reached a steady state, and further refinement in terms of the number of material points may not be necessary to better predict the r-value. Indeed, results from the base numerical discretization may be trusted, and perhaps more desirable due to the decrease in computation time.

3.3. Effect of the number of grains

As the number of grains within a domain is increased, the behavior of the average r-value is not easily described. In the AA6016 sample, there seems to be a slightly positive correlation

Table 5. Maximum changes to the average r-value, calculated as the maxima of the absolute differences between the average r-values in each parameter set, considering all sample inclinations. The in-plane inclination angles at which the maxima occur are in parentheses.

	$\Delta r^{\max}$	
Parameter	AA6016	AA5182
ξ_0	0.0117 (45°)	0.0090 (90°)
ξ_∞	0.0119 (45°)	0.0098 (90°)
$h_{\alpha\beta}$	0.0297 (0°)	0.0157 (0°)
n	0.0256 (0°)	0.0228 (0°)
Material points	0.0190 (45°)	0.0327 (0°)
Grains	0.0294 (0°)	0.0213 (67.5°)
Texture sampling	0.1612 (45°)	0.1125 (45°)

(though not generally so). In the AA5182 sample, there is perhaps a slightly negative correlation (though, again, not generally so). While we expect a behavior similar to that witnessed when the numerical discretization is increased—that is, a saturation toward a steady state as the number of grains is increased—the trends do not indicate such a behavior. This is likely due to two reasons. Firstly, as the number of grains is increased, the intra-grain refinement decreases, as the level of numerical discretization is held constant (in this case at 32^3). Secondly, as the number of grains is increased, the grain statistics improve (i.e., the overall texture of the virtual sample will more closely match that of the experimental sample). The interplay of these two conditions is not readily understood from the data gathered in this study, and requires investigation in a separate study. As such, it is difficult to say definitively the number of grains necessary to reach a steady state response—though again, the differences between the two samples (AA6016 shows greater changes in the r-value than the AA5182, which may be reaching steady state) indicate that this is likely influenced by crystallographic texture.

3.4. Effect of initial crystallographic texture

Changes to the initial crystallographic texture of the sample have the largest impact on the prediction of the r-value. Figure 14 indicates that the r-value is heavily dependent on changes to the initial texture—or, in the case of this figure, the changes to the texture through the thickness of the sample. Indeed, the largest changes in the average r-value as summarized in table 5 occur due to changes in initial texture, which command the ability to sway the r-value by values an order of magnitude greater than any of the other variables considered in this study. Inspecting figure 14, note how not only the magnitude of the r-value changes as the initial texture is altered, but so does the degree of in-plane anisotropy. For instance, the AA6016 sample experiences a more isotropic response when considering the texture on the outer surface of the sheet, whereas the AA5182 sample experiences a higher degree of in-plane anisotropy when considering the same texture regions (and vice versa when considering the innermost regions of the sheet).

4. Conclusions

In summary, a suite of simulations is performed in which the degree of plastic anisotropy—quantified via the r-value—is predicted for two aluminum alloys. Simulation

parameters are systematically altered to determine their influence on the predicted sheet behavior. Namely, parameters governing the slip and hardening response of the material, numerical parameters, and geometric discretization are considered. A total of 1600 simulations are performed to provide statistics for each parameter set. Overall, results show that:

- changes in the hardening assumption (latent, direct, or isotropic) and strain-rate sensitivity have a larger effect on the predicted *r*-value than changes of the initial slip system strength or the saturation strength. These changes, however, are small when compared to those from variations to the initial texture;
- the sensitivity of the *r*-values to changes of the hardening parameters is larger for AA6016 than for AA5182. This result indicates, that the sensitivity may be generally higher for pronounced textures than for balanced textures;
- as numerical discretization is increased, the average predicted *r*-value tends to saturate and the spread in predicted values decreases (though not generally so), while the spread in the data tends to decrease (though not generally so);
- as the number of grains is increased, the average predicted *r*-value, as well as the spread in the data, show few discernible trends. Certainly, to investigate small changes of the *r*-value, it is necessary to perform repeated simulations on multiple samples of the texture to gain meaningful results.

Overall, this study demonstrates that a reasonable estimate in the majority of crystal plasticity modeling parameters will yield a reasonable prediction of plastic anisotropy of rolled sheet. Accurate quantification of microstructure (primarily crystallographic texture), and the determination of an appropriate hardening assumption are necessary to determine a sheet's *r*-value, whereas other modeling parameters (other slip and plasticity parameters) have little influence on the bulk deformation response.

Acknowledgments

Sheet samples and experimental tensile data were provided by Austria Metall AG. Special thanks to Christian Broß and Stefan Zaefferer for performing electron backscatter diffraction measurements, and to Markus Kühbach for providing efficient post-processing solutions necessary for such a large number of simulations (all of the Max-Planck-Institut für Eisenforschung GmbH).

Author contribution

MK, GF, and FR conceived of the topic. MK planned and performed all simulations and post-processing, as well as main authorship of this manuscript. GF contributed to facilitating materials, experimental tensile testing, and authorship of this manuscript. FR contributed to authorship of this manuscript, technical discussion, and overall project guidance.

ORCID iDs

M Kasemer https://orcid.org/0000-0001-8355-7733
G Falkinger https://orcid.org/0000-0002-2959-6835
F Roters https://orcid.org/0000-0002-9098-9566

References

[1] AMAG Austria Metall AG 2018 Internal market analysis
[2] Graf A and Hosford W 1990 Calculations of forming limit diagrams *Metall. Trans.* A **21** 87–94
[3] Butuc M, Gracio J and da Rocha A B 2003 A theoretical study on forming limit diagrams prediction *J. Mater. Process. Technol.* **142** 714–24
[4] Ahmadi S, Eivani A and Akbarzadeh A 2009 Experimental and analytical studies on the prediction of forming limit diagrams *Comput. Mater. Sci.* **44** 1252–7
[5] Volkswagen A G 2010 6xxx series aluminum alloy sheets technical specification TL094
[6] ISO Central Secretary 2006 *Metallic Materials–Sheet and Strip–Determination of Plastic Strain Ratio Standard* (Geneva: International Organization for Standardization)
[7] Mathur K K and Dawson P R 1989 On modeling the development of crystallographic texture in bulk forming processes *Int. J. Plast.* **5** 67–94
[8] Mathur K K, Dawson P R and Kocks U 1990 On modeling anisotropy in deformation processes involving textured polycrystals with distorted grain shape *Mech. Mater.* **10** 183–202
[9] Dawson P R, MacEwen S R and Wu P-D 2003 Advances in sheet metal forming analyses: dealing with mechanical anisotropy from crystallographic texture *Int. Mater. Rev.* **48** 86–122
[10] Khadyko M, Maiorara C, Dumoulin S, Rvik T B and Hopperstad O 2017 Effects of heat-treatment on the plastic anisotropy of extruded aluminium alloy AA6063 *Mater. Sci. Eng.* A **708** 208–21
[11] Engler O, Schäfer C and Myhr O 2015 Effect of natural ageing and pre-straining on strength and anisotropy in aluminium alloy AA6016 *Mater. Sci. Eng.* A **639** 65–74
[12] Khadyko M, Dumoulin S, Cailltaud G and Hoppestad O 2016 Latent hardening and plastic anisotropy evolution in AA6060 aluminium alloy *Int. J. Plast.* **76** 51–74
[13] Zecevic M and Knezevic M 2018 Latent hardening within the elasto-plastic self-consistent polycrystal homogenization to enable the prediction of anisotropy of AA6022-T4 sheets *Int. J. Plast.* **105** 141–63
[14] Roters F, Eisenlohr P, Hantcherli L, Tjahjanto D, Bieler T and Raabe D 2010 Overview of constitutive laws, kinematics, homogenization and multiscale methods in crystal plasticity finite-element modeling: theory, experiments, applications *Acta Mater.* **58** 1152–211
[15] Dawson P R and Boyce D E 2015 FEpX–finite element polycrystals: theory, finite element formulation, numerical implementation and illustrative examples arXiv:1504.03296
[16] Wong S and Dawson P 2010 Influence of directional strength-to-stiffness on the elastic–plastic transition of fcc polycrystals under uniaxial tensile loading *Acta Mater.* **58** 1658–78
[17] Kasemer M, Quey R and Dawson P 2017 The influence of mechanical constraints introduced by β annealed microstructures on the yield strength and ductility of Ti–6Al–4V *J. Mech. Phys. Solids* **103** 179–98
[18] Moulinec H and Suquet P 1998 A numerical method for computing the overall response of nonlinear composites with complex microstructure *Comput. Methods Appl. Mech. Eng.* **157** 69–94
[19] Lebensohn R A, Kanjarla A K and Eisenlohr P 2012 An elasto-viscoplastic formulation based on fast fourier transforms for the prediction of micromechanical fields in polycrystalline materials *Int. J. Plast.* **32–33** 59–69
[20] Roters F *et al* 2019 DAMASK–the düsseldorf advanced material simulation kit for modeling multi-physics crystal plasticity, thermal, and damage phenomena from the single crystal up to the component scale *Comput. Mater. Sci.* **158** 420–78
[21] Delannay L, Melchior M, Signorelli J, Remacle J-F and Kuwabara T 2009 Influence of grain shape on the planar anisotropy of rolled steel sheets–evaluation of three models *Comput. Mater. Sci.* **45** 739–43
[22] Hu L, Rollett A, Iadicola M, Foecke T and Banovic S 2012 Constitutive relations for AA5754 based on crystal plasticity *Metall. Mater. Trans.* A **43** 854–69
[23] Bachmann F, Hielscher R and Schaeben H 2010 Texture analysis with MTEX–free and open source software toolbox *Solid State Phenom.* **160** 63–8
[24] Wielewski E, Boyce D E, Park J-S, Miller M P and Dawson P R 2017 A methodology to determine the elastic moduli of crystals by matching experimental and simulated lattice strain pole figures using discrete harmonics *Acta Mater.* **126** 469–80
[25] Dawson P R, Boyce D E, Park J-S, Wielewski E and Miller M P 2018 Determining the strengths of HCP slip systems using harmonic analyses of lattice strain distributions *Acta Mater.* **144** 92–106

[26] Kasemer M, Echlin M P, Stinville J C, Pollock T M and Dawson P 2017 On slip initiation in equiaxed α/β Ti–6Al–4V *Acta Mater.* **136** 288–302
[27] Kasemer M, Zepeda-Alarcon E, Carson R, Dawson P and Wenk H-R 2020 Deformation heterogeneity and intragrain lattice misorientation in high strength contrast, dual-phase bridgmanite/periclase *Acta Mater.* **189** 284–98
[28] Engler O and Hirsch J 2002 Texture control by thermomechanical processing of AA6xxx Al–Mg–Si sheet alloys for automotive applications—a review *Mater. Sci. Eng.* A **336** 249–62
[29] Vatne H, Furu T and Nes E 1996 Nucleation of recrystallized grains from cube bands in hot deformed commercial purity aluminum *Mater. Sci. Technol.* **12** 201–10
[30] Samajdar I and Doherty R 1998 Cube recrystallization texture in warm deformed aluminum: understanding and prediction *Acta Mater.* **46** 3145–58
[31] Falkinger G, Regl K and Mitsche S 2019 Recrystallized cube grains in an Al–Mg–Si alloy dependent on prioir cold rolling *Mater. Sci. Technol.* **35** 1081–7
[32] Dillamore I and Katoh H 1974 The mechanics of recrystallization in cubic metals with particular reference to their orientation-dependence *Met. Sci.* **8** 73–83
[33] Akef A and Driver J 1991 Orientation splitting of cube-oriented face-centered cubic crystals in plane strain compression *Mater. Sci. Eng.* A **132** 245–55
[34] Sidor J, Decroos K, Petrov R and Kestens L 2015 Evolution of recrystallization textures in particle containing Al alloys after various rolling reductions: experimental study and modeling *Int. J. Plast.* **66** 119–37
[35] Engler O 2002 Through-process modelling of the impact of intermediate annealing on texture evolution in aluminum alloy AA5182 *Modelling Simul. Mater. Sci. Eng.* **11** 863–82
[36] Humphreys J, Rohrer G and Rollett A 2017 *Recrystallization and Related Annealing Phenomena* (Amsterdam: Elsevier)
[37] ISO Central Secretary 2016 *Metallic Materials—Tensile Testing—Part 1: Method of Test at Room Temperature, Standard* (Geneva: International Organization for Standardization)
[38] Nye J F 1985 *Physical Properties of Crystals: Their Representation by Tensors and Matrices* (Oxford: Oxford University Press)
[39] Lu C, Deng G, Tieu A, Su L, Zhu H and Liu X 2011 Crystal plasticity modeling of texture evolution and heterogeneity in equal channel angular pressing of aluminum single crystal *Acta Mater.* **59** 3581–92
[40] Inal K, Mishra R K and Cazacu O 2010 Forming simulation of aluminum sheets using an anisotropic yield function coupled with crystal plasticity theory *Int. J. Solids Struct.* **47** 2223–33
[41] Ayachit U 2015 *The ParaView Guide: A Parallel Visualization Application* (Clifton Park, NY: Kitware)
[42] Engler O 2015 Texture and anisotropy in cold rolled and recovery annealed AA5182 sheets *Mater. Sci. Technol.* **31** 1058–65
[43] Carson R, Obstalecki M, Miller M and Dawson P 2017 Characterizing heterogeneous intragranular deformations in polycrystalline solids using diffraction-based and mechanics-based metrics *Modelling Simul. Mater. Sci. Eng.* **25** 055008